Folding in and out: passive morphing in flapping wings

2015 Bioinspir. Biomim. 10 025001

(http://iopscience.iop.org/1748-3190/10/2/025001)

Bioinspiration & Biomimetics

PAPER

Folding in and out: passive morphing in flapping wings

RECEIVED
10 May 2014

ACCEPTED FOR PUBLICATION
11 September 2014

PUBLISHED
25 March 2015

Amanda K Stowers and David Lentink

Department of Mechanical Engineering, Stanford University, Stanford, CA 94305, USA

E-mail: astowers@stanford.edu

Keywords: bioinspired, flapping wings, wing morphing, underactuated, sweep, animal flight

Supplementary material for this article is available online

Abstract

We present a new mechanism for passive wing morphing of flapping wings inspired by bat and bird wing morphology. The mechanism consists of an unactuated hand wing connected to the arm wing with a wrist joint. Flapping motion generates centrifugal accelerations in the hand wing, forcing it to unfold passively. Using a robotic model in hover, we made kinematic measurements of unfolding kinematics as functions of the non-dimensional wingspan fold ratio (2–2.5) and flapping frequency (5–17 Hz) using stereo high-speed cameras. We find that the wings unfold passively within one to two flaps and remain unfolded with only small amplitude oscillations. To better understand the passive dynamics, we constructed a computer model of the unfolding process based on rigid body dynamics, contact models, and aerodynamic correlations. This model predicts the measured passive unfolding within about one flap and shows that unfolding is driven by centrifugal acceleration induced by flapping. The simulations also predict that relative unfolding time only weakly depends on flapping frequency and can be reduced to less than half a wingbeat by increasing flapping amplitude. Subsequent dimensional analysis shows that the time required to unfold passively is of the same order of magnitude as the flapping period. This suggests that centrifugal acceleration can drive passive unfolding within approximately one wingbeat in small and large wings. Finally, we show experimentally that passive unfolding wings can withstand impact with a branch, by first folding and then unfolding passively. This mechanism enables flapping robots to squeeze through clutter without sophisticated control. Passive unfolding also provides a new avenue in morphing wing design that makes future flapping morphing wings possibly more energy efficient and light-weight. Simultaneously these results point to possible inertia driven, and therefore metabolically efficient, control strategies in bats and birds to morph or recover within a beat.

1. Introduction

Animals are capable of more extreme maneuvering in complex environments than man-made aerial robots. While there are many differences between flying animals and flying robots, a prominent one is that natural flyers are capable of wing morphing during flight (Carruthers *et al* 2007, Lentink *et al* 2007, Pennycuick 1968). Bats use an articulated skeleton covered by an elastic membrane under active muscular control (Song *et al* 2008, Swartz *et al* 2007) to morph their wings, but wing folding is limited by membrane slacking (Pennycuick 2008). In contrast, birds can morph their wings until they are tucked against the body, while maintaining a high-performance aerodynamic shape, due to overlapping feathers under musculoskeletal control (Pennycuick 2008). Such extreme wing morphing allows for impressive feats of maneuverability, such as flying through brush with gaps barely larger than the body. Further, extreme morphing allows pigeons (Pennycuick 1968) and swifts (Lentink *et al* 2007) to increase efficiency by adjusting wingspan while flying at a wide range of speeds to take advantage of optimum glide conditions. In eagles, passive wing morphing helps prevent flow separation and improve lift (Carruthers *et al* 2007), suggesting passive wing morphing mechanisms are important in bird flight.

Bird wings are anatomically homologous to human arms in that they have portions corresponding

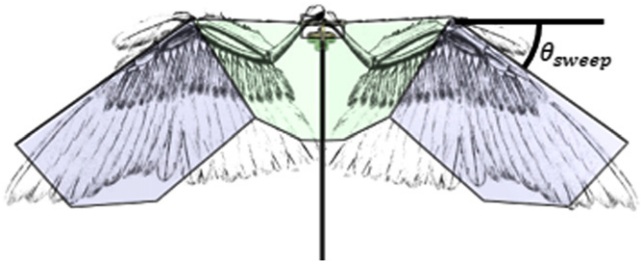

Figure 1. Comparison of our robot and bird wing morphology. At the wrist, the bird and robot are able to rotate their wings to adjust the sweep angle. The robot features a bird-inspired wrist joint that connects the arm and hand wings with a rotational degree of freedom that allows it to sweep forwards (unfold) and backwards (fold). Bird wings from 'Illustrations of Zoology' (Smith and Norwell 1889).

to an upper arm, lower arm, and hand. The wings connect to the body through the shoulder joint, which is activated by several muscles. In a cockatoo, the pectoralis, biceps and extensor metacarpi radialis activate to begin the downstroke, while the supracoracoideus activates to finish the downstroke (Hedrick and Biewener 2007). The elbow and hand joints are located distally and form a V-shape under muscular control. During flight, birds can manipulate these joints to adjust wing sweep and independently fold each wing. How wing morphing, particularly sweep, is controlled within a beat is poorly understood in birds (Altshuler *et al* 2012, Hedrick and Biewener 2007, Hedrick *et al* 2007), and in animal flight in general (Taylor *et al* 2012). Out of necessity, engineers have developed a myriad of bio-inspired robots based on mostly anecdotal information of wing morphing musculoskeletal control in bats and birds.

There exist at least three different lineages of bio-inspired morphing wings (1) non-flapping wings that morph, (2) flapping wings that morph passively through aeroelastic coupling, and (3) flapping wings that deform in part passively through aeroelastic coupling, and in part through active control.

Examples of robots that use morphing wings without flapping to achieve greater flight efficiency include the RoboSwift (Team Roboswift 2007). This robot has a hand wing consisting of four overlapping carbon fiber feathers that enables it to sweep its wings back and forth to extend its performance like a gliding swift. Unlike some other biomimetic robots or flying animals, the RoboSwift generates its thrust with a nose mounted propeller. However, the wing sweep and area is under tight control to optimize flight performance at different speeds. Adjusting wing sweep has also been used for control. A seagull inspired robot from the University of Florida controls the sweep of both the arm and hand wings using biomimetic shoulder and elbow joints (Grant *et al* 2006). Control of the joint angles enables variation of wing shape and area (Grant *et al* 2010). This enables them to reduce turn radius and better reject crosswinds. Another vehicle from the same group controls the dihedral angle to achieve similar results. Birds are capable of controlling both sweep and dihedral.

Some newer robots have been developed that control their flight by manipulating their wing kinematics. For instance, the Nano-Hummingbird (Keennon *et al* 2012) is a 19 gram flapping winged vehicle which attains controlled flight without a tail, using only the wings for control surfaces. By adjusting the angle of attack of each wing through variable tension, it is able to control roll, pitch, and yaw. Another flapping robot takes advantage of passive wing dihedral morphing to increase flight efficiency (Wissa *et al* 2012). Its wing has a joint at approximately the wrist location of the leading edge, which modifies wing dihedral. The joint is compliant in one direction but not the other, so the dihedral becomes negative and wingspan decreases during the upstroke. In contrast, dihedral remains unchanged and wing span is fully extended during the downstroke. The change in wingspan throughout the wingbeat results in an increase in lift and a decrease in power compared to a wing without such a joint.

Advanced wind tunnel models demonstrate how flapping wings can morph in more sophisticated ways by combining active and passive mechanisms. These models utilize a flexible membrane controlled by an articulated skeleton inspired by bats (Colorado *et al* 2012, Bahlman *et al* 2013). The robots change wing shape dynamically using either shape memory alloy muscle wires or servomotors that actuate artificial tendons running across pulleys in the joints. This provides them with the capability to control force and torque by manipulating wing shape and inertia within a beat for low flapping frequencies (Colorado *et al* 2012, Bahlman *et al* 2013). While the wing membrane deforms in part passively through aeroelastic coupling, wing sweep and area are tightly controlled.

None of these advanced morphing robots demonstrate passive morphing mechanisms for wing folding. Passive wing unfolding has been demonstrated in folding propellers. They unfold through centrifugal accelerations that change dihedral, and force the propeller to be fully extended at high angular velocities, like the Watts governor (Maxwell 1867, MacKenzie and Forrester 2008, Deters and Selig 2008). These propellers

rely on changing dihedral and not on changing wing sweep. Self-feathering propellers also adjust their propeller pitch automatically, but do not adjust the total swept area. Changing wing sweep like a bird (figure 1) involves folding the hand and arm wing and provides exquisite control over wing shape and area that is currently not available in flapping robots.

Here we present results for a flapping morphing wing based on experiments, a predictive dynamical model and dimensional analysis of a wing that unfolds passively. The unfolding changes wing sweep, shape and area in concert. The morphing wing is inspired by both bird and bat wings. The ability to fold the hand wing over the arm wing using an origami fold resembles the shape change obtained with the overlapping feathers of birds, while the membrane resembles that of bats. The goal of our study is to demonstrate how flapping wings can unfold about the wrist joint without additional actuation beyond the wings' periodic flapping motion. We built a model robot with pin joints at the wrists and made kinematic measurements of flap and fold angle for a selection of wing sizes and flapping frequencies. Using carbon fiber and Mylar with custom 3d printed joints it was possible to create an exceptionally light-weight morphing mechanism that adds only 3% of the total weight of a similar flapping wing micro air vehicle, without such a mechanism (Lentink *et al* 2009). We found experimentally that the flapping motion caused unfolding in about one to two flaps for relatively small flapping amplitudes. A simulation incorporating effects of inertia, mechanical contact, and simple estimates of aerodynamic forces was able to predict the general shape of the unfolding sequence. The simulation enabled us to test the effect of larger flapping amplitudes on unfolding time, which can be less than half a wingbeat. The effect of scale on the period of the folding sequence was subsequently analyzed using a dimensional analysis. These results all suggest that the wing unfolding can be performed across scales using under actuated strategies based on centrifugal acceleration, which may reduce actuator weight in future flying robots. The result also alludes to possible semi-passive morphing strategies for unfolding wings in flapping animal flight. Finally, we tested wing unfolding after a major collision with a branch like structure, a high-velocity rod, which shows that the passive wing unfolding mechanism withstands high-impact collisions and facilitates an automatic response that fully unfolds the wing within about a beat. This enables future flapping robots to squeeze between branches and clutter with less sophisticated control algorithms as the wings can passively deal with hard contact. The results also suggests that the flapping motion generated by the two major flight muscles, the pectoralis and supracoracoideus, induce passive unfolding accelerations that probably help bat and bird wings unfold after the upstroke, impact with a branch, or the wing of a flock member.

2. Experimental methods

2.1. Mechanical wing design and construction

The wing design is a standard carbon fiber and Mylar variety based off earlier DelFly designs (Lentink *et al* 2009). To enable folding the wings fully, the arm wing leading edge must be longer than the maximum chord length. We chose wings with a greater aspect ratio because the arm wing must be fairly rigid in order to prevent wing tangling, which probably sacrifices some lift.

Wing sets were constructed from 5 μm thick Mylar foil with D-shaped carbon fiber leading edges (1 mm radius arm wing, 0.8 mm radius hand wing). The wing was stiffened using 0.28 mm diameter round carbon fiber spars attached with Weldwood Contact Cement. Carbon fiber components were connected using cyanoacrylate and 3d printed wing attachments and joints (Projet 3500 UHD, 29 μm layers). Each wing had a pin joint mid-wing to simulate the wrist. This joint allows a degree of freedom in the sweep direction. When the wings flap, the hand wings unfold automatically.

2.2. Structure and measurement parameters

To assess how wing unfolding occurs in a robot, we measured unfolding characteristics over a range of wing sizes and flapping frequencies (5–17 Hz) while bolted to a table with zero forward velocity, as if hovering. Power was supplied directly to an 8 mm model helicopter motor (HK189A) geared down 12:1. We define the fold ratio (figure 2) as the ratio of fully folded wingspan to fully unfolded wingspan:

$$\text{fold ratio} = \frac{\text{fully unfolded wingspan}}{\text{fully folded wingspan}} \equiv \frac{l_{\text{arm}} + l_{\text{hand}}}{l_{\text{arm}}}. \quad (1)$$

Three fold ratios (2.0, 2.2, and 2.5) were selected to study the effect of fold ratio on wing unfolding. We chose wings with the smallest folding ratio to test the effect of the moment of release, because these wings morphed the most. We chose the nominal 14 Hz flapping frequency because this frequency is needed to support the weight of a DelFly-like flapping robot of similar scale (Lentink *et al* 2009). For consistency, the same flapping mechanism was used in all wings, corresponding to identical flapping amplitudes and offsets. Each set of wings had a 400 mm wingspan with an 80 mm chord length (figure 3). The wing spars' positions and lengths were scaled according to the radius of the hand wing to correspond geometrically with DelFly wings (Lentink *et al* 2009, Bruggeman 2010) .

The hand wings were held in place prior to release by a Kevlar string attached to a custom servo horn. The string was threaded through a figure-8 loop at the front of the wings, and tied to a wire on each hand wing. Upon pressing a button, an indicator LED turned on and a high speed servo (0.032 s/60 deg @7.4 V, Savox SB2272MG) moved the string quickly to the fully forward position. The high speed servo ensured that the release system dynamics would be

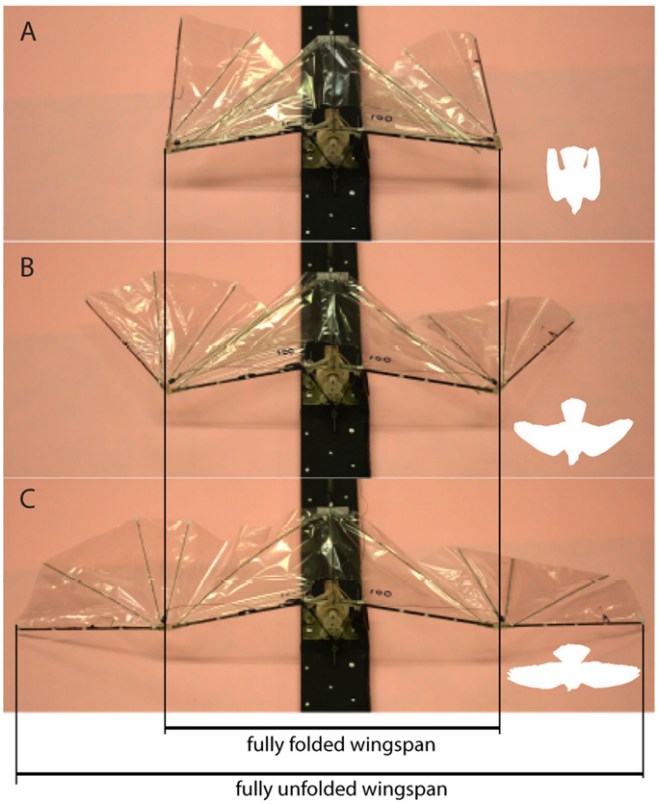

Figure 2. The robot in fully folded (A) and extended (C) configuration showing the definition of the fold ratio. Robot photographed in static configurations. Pigeon outlines derived from Pennycuick (Pennycuick 1968).

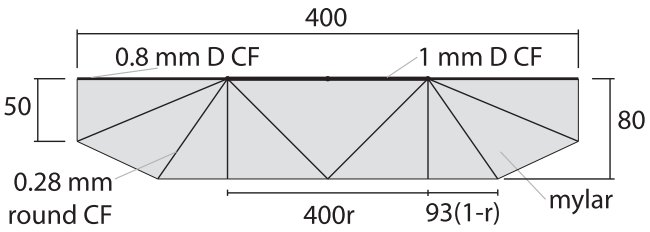

Figure 3. Wings were constructed with carbon fiber leading edges and spars, Mylar foils and 3d printed joints. We built three wing sets with folding ratios of 2, 2.2 and 2.5. Each wing set had a wingspan of 400 mm and a chord length of 80 mm. Other dimensions were scaled accordingly.

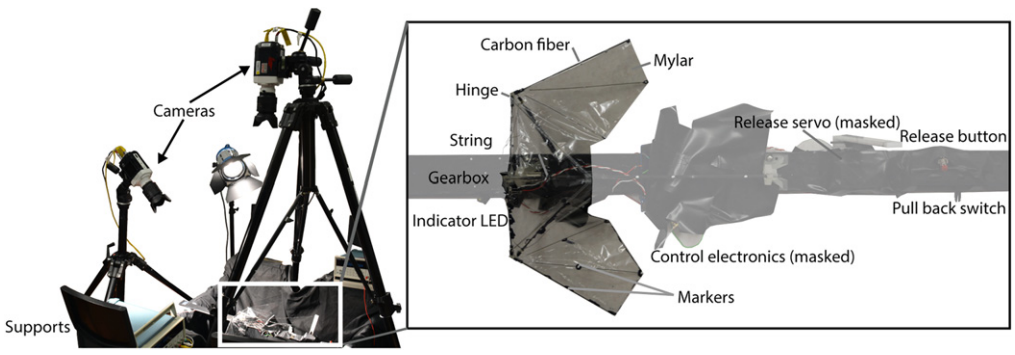

Figure 4. Three-dimensional high-speed motion tracking setup. The robot consists of a pair of carbon fiber and Mylar hinged wings mounted to a piece of aluminum. A high-speed servo system released the wings. Markers and LEDs allow measurement of kinematics. Strings constrain the wing from unfolding until released.

significantly faster than the wing unfolding dynamics. At an estimated flapping frequency of 14 Hz, the release time (~16 ms) corresponds to approximately 22% of a wingbeat, which is significantly faster than the predicted unfold time and the unfold time measured using cutting the string. We did not use cutting the string as a final release mechanism because it was destructive to the release wire.

2.3. Measuring flap and fold angles

We reconstructed kinematic data from high-speed (500 fps) recordings of fixed markers on the unfolding motion (see figure 4). Two cameras (Phantom Miro M310) were calibrated using DLT software (Hedrick 2008) with an average DLT error of less than 2%. Fixed points were digitized around the horizontal aluminum surface that supported the robot and the carbon fiber body to provide reference vectors. Five markers were placed along the leading edge of each of the arm and hand wing. Two markers were placed along each of the three spars on each wing for angle of attack measurements.

3. Dynamic model of passive morphing

3.1. Wing sweep dynamics model with aerodynamic effects

The wings are assumed to consist of two rigid bodies—the arm wing and the hand wing. For the purposes of calculating moment of inertia, each body is assumed to have the mass of the carbon fiber rods concentrated in the leading edge, and the mass of the Mylar spread evenly over a rectangular hand wing surface. The arm wings are attached to the body through a pin joint enabling flapping. The body is fixed with zero velocity as if in hover. The model is created in MotionGenesis software (max integration step 0.001 s, absolute tolerance 1e-8, and relative tolerance 1e-8). In the model, the arm wings flap with amplitude θ_{flap}, that is set to match experimental data. The hand wing is assumed to have two degrees of freedom. The first is a twist angle which is driven sinusoidally out of phase with the flap angle to simulate the inertial and aerodynamic effects of wing deformation. The second is the sweep angle which allows the hand wing to rotate about an axis perpendicular to the flapping axis of the arm wing. The hand wing is unconstrained in this direction until it reaches the unfolded position. At the fully unfolded position, we simulate contact using a spring-damper that captures the combined effect of the Mylar's response to stretch and the plastic parts contacting each other (common contact method as in Gilardi and Sharf 2002). Finally we integrate aerodynamic forces in our model using a quasi-steady model of a flapping wing to estimate lift and drag (Dickinson *et al* 1999). This aerodynamic model represents the order of magnitude of the aerodynamic force, but also ignores many components, which is acceptable because we found that inertial effects dominate passive wing unfolding.

3.2. Quasi-steady aerodynamic model of the flapping wing

The aerodynamic model is based on the quasi-steady model for flapping wings ignoring rotational lift, wake-capture and added mass amongst other effects (Dickinson *et al* 1999). The quasi-steady model predicts the aerodynamic forces for the instantaneous angle of attack, flapping velocity, and wing shape, based on measurements of the aerodynamic force for the same parameters with a revolving wing (Dickinson *et al* 1999, Dickinson *et al* 2008). The wing's angle of attack is formed by a combination of the flapping angle, twist angle, and fold angle. In this approximation we assume that the values measured for fly wings by Dickinson *et al* (1999) are sufficiently accurate for our analysis, which our simulations support, because the influence of aerodynamics on unfolding is negligible compared to wing inertia (figure 9).

$$\begin{aligned} C_L &= 0.225 + 1.58 \sin(2.13\alpha - 7.20) \\ C_D &= 1.92 + 1.55 \cos(2.04\alpha - 9.82) \end{aligned}. \quad (2)$$

The drag acts parallel to, and in the opposite direction of, the velocity calculated at the center of pressure. The lift acts in a direction perpendicular to both the drag and the vector leading perpendicularly from the spar to the center of pressure. The choice of direction is then chosen based off whether the wing is in the up or down stroke such that it supports the hovering motion demonstrated with earlier flapping wing robots (Lentink *et al* 2009).

The aerodynamic forces generated by the flapping wing are assumed to act at the radius of gyration, the wings center of aerodynamic pressure, which is calculated at each time step to account for wing morphing. The actual location of the radius of gyration depends on the magnitude of the ratio of the arm to hand wing angular velocities. To implement this in our dynamic model we had to assume a constant ratio, for which we selected one, so the flapping and wing sweep angular velocity are assumed to be identical for the calculation of the approximate radius of gyration. This assumption is based on the outcome of our dimensional analysis that shows the flapping and unfolding period are about equal, which has been confirmed by our experiments and simulations. The radius of gyration and the fold angle are related using a quadratic best fit approximation. Chordwise, the force is applied at one-quarter chord length from the leading edge to the trailing edge (Deng *et al* 2006).

3.3. Effects of inertia on underactuated sweep angle

The inertia model of our flapping morphing wing is analogous to a driven double pendulum (figure 5) with perpendicular axes (Bridges and Georgiou 2001) as the sweep axis is perpendicular to the flapping axis. The

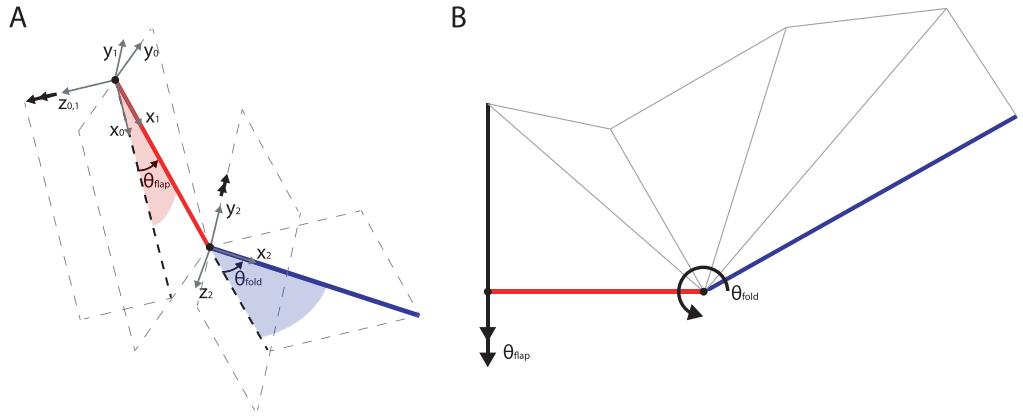

Figure 5. Correspondence between double pendulum and the folding wing design. (A) Double pendulum model showing leading edges and flap and fold angles. (B) The flap angle is driven sinusoidally and the fold angle is free to rotate until it is fully unfolded (fold angle of 7°). Top view of folding wing with spars and Mylar edges shown.

flapping angle is specified; therefore there is only one degree of freedom, the sweep axis that facilitates wing folding. The equation for the fold angle under these assumptions is:

$$\ddot{\theta}_{\text{fold}} = \frac{-\sin\left(\theta_{\text{fold}}\right)}{2I_{yy}}\left\{\left[L_{\text{inner}}L_{\text{outer}}m + 2\left(I_{zz}-I_{xx}\right)\cos\left(\theta_{\text{fold}}\right)\right]\left(\dot{\theta}_{\text{flap}}\right)^2 - L_{\text{outer}}mg\,\sin\left(\theta_{\text{flap}}\right)\right\}. \quad (3)$$

The equation consists of two parts, accelerations due to flapping motion and due to gravity. The unfolding process starts at the fully folded position for which θ_{fold} is almost 90°, because the wing needs an infinitesimal perturbation to start unfolding. The unfolding is driven by the angular centrifugal acceleration induced by the angular velocity due to flapping (the first term between brackets). If we ignore the effect of gravity (the second term) we see that the second derivative of the folding angle will be negative throughout the flapping cycle, until the wing is unfolded. This negative angular acceleration results in negative angular velocity that causes the wing to move towards the unfolded position. This effect increases with flapping frequency squared. The gravity term is capped by the maximum flapping angle, so it is always possible to flap fast enough to overcome its effects and unfold the wing. Faster flapping leads to faster unfolding of the wing. Within the unfolding process, the unfolding acceleration reaches its maximum at mid-stroke when flapping angular velocity is maximum.

3.4. Non-dimensional analysis of passive unfolding

Dimensional analysis shows that flapping effects dominate over gravitational effects and that the time to unfold is on the same order of magnitude as flapping period. Using the double pendulum equations, we can analyze how wing parameters affect passive wing unfolding time. First, we assume that the wing flaps and unfolds sinusoidally. This can be expressed as:

$$\theta_{\text{flap}} = \theta^0_{\text{flap}}\sin 2\pi f_{\text{flap}}t. \quad (4)$$

$$\theta_{\text{fold}} = \theta^0_{\text{fold}}\cos 2\pi f_{\text{fold}}t. \quad (5)$$

Then, we can normalize the flapping velocity and folding accelerations by their maximum values, substituting in:

$$\ddot{\theta}_{\text{fold}} = \theta^0_{\text{fold}}(\pi f_{\text{fold}})^2\,\ddot{\theta}^{\star}_{\text{fold}}. \quad (6)$$

$$\dot{\theta}_{\text{flap}} = \theta^0_{\text{flap}}2\pi f_{\text{flap}}\dot{\theta}^{\star}_{\text{flap}}. \quad (7)$$

Then we must make one other assumption and some definitions. First, we assume that the hand wing mass distribution consists of a leading edge with 2/3 the total mass, a flat plate for the membrane with 1/6 the total mass, and 1/12 of the mass in each spar, giving us expressions for the moments of inertia. We define an AR for a single hand wing

$$\frac{1}{AR} = \frac{c}{L_{\text{hand}}}. \quad (8)$$

Substituting in these values and simplifying, we obtain the equation

$$\ddot{\theta}^{\star}_{\text{fold}} = \frac{-576\left(\theta^0_{\text{flap}}\right)^2}{\left(3\left(\frac{1}{AR}\right)^2+11\right)\pi}\left[\frac{FR}{FR-1}+\frac{11}{18}-\frac{1}{6}\left(\frac{1}{AR}\right)^2\right] \times\frac{f^2_{\text{flap}}}{f^2_{\text{fold}}}\left(\dot{\theta}^{\star}_{\text{flap}}\right)^2+\frac{144g}{\pi^3 f^2_{\text{fold}}L_{\text{hand}}\left(3\left(\frac{1}{AR}\right)^2+11\right)}, \quad (9)$$

where the first term refers to the effects of flapping, and the second to the effects of gravity. We define these terms as

$$\pi_1 = \frac{-576\left(\theta^0_{\text{flap}}\right)^2}{\left(3\left(\frac{1}{AR}\right)^2 + 11\right)\pi}\left[\frac{FR}{FR-1} + \frac{11}{18} - \frac{1}{6}\left(\frac{1}{AR}\right)^2\right] \times \frac{f^2_{\text{flap}}}{f^2_{\text{fold}}}$$

$$\pi_2 = \frac{144g}{\pi^3 f^2_{\text{fold}} L_{\text{hand}}\left(3\left(\frac{1}{AR}\right)^2 + 11\right)}. \quad (10)$$

With representative values plugged in $\left(\theta^0_{\text{flap}} = \frac{\pi}{9}, = 14\text{HZ}, \quad L_{\text{hand}} = 0.12\text{ m}, \quad FR = 2.5, \left(\frac{1}{AR}\right) = \frac{0.08\text{ m}}{0.12\text{ m}} = \frac{2}{3}\right)$, we obtain that the ratio of π_1 to π_2 is approximately 14 (the f_{fold} terms cancel in the ratio), so the effects of gravity are an order of magnitude smaller than the effects of flapping. The effect of gravity can thus be ignored. The only dependency on length scale is in the denominator of the gravity term. Given that flapping frequency must increase as wingspan decreases (Lentink *et al* 2009), the gravity term will be much smaller than the flapping term for bird and bat scales as well as smaller species such as insect sized. Therefore we can relate the folding frequency to flapping frequency, flapping amplitude, fold ratio and aspect ratio. We can make the wing unfold faster by doing one of the following:

1. Increasing the flapping frequency,
2. Increasing the flapping amplitude,
3. Decreasing the fold ratio,
4. Increasing the hand wing aspect ratio.

Increasing the flapping frequency (1) decreases the absolute unfold time. Increasing flapping amplitude (2), fold ratio (3) and aspect ratio (4) decrease the relative unfold time.

Both fold ratio (3) and inverse aspect ratio (4) are roughly equal to order of magnitude one and cannot be changed beyond this order of magnitude. Increases in flapping frequency (1) and amplitude (2) result in higher angular velocities, leading to shorter unfold times. Given that fold ratio, aspect ratio and flapping amplitude cannot be varied over more than approximately one order of magnitude, we can approximate them by typical values $\left(FR = 2, \frac{1}{AR} = 1\right)$ to find a relationship between the flap and fold frequencies:

$$\pi_1 = \frac{-576(\pi/9)^2}{(14)\pi}\left[\frac{22}{9}\right]\frac{f^2_{\text{flap}}}{f^2_{\text{fold}}} = -3.9\frac{f^2_{\text{flap}}}{f^2_{\text{fold}}}. \quad (11)$$

Since we know π_1 is order of magnitude one, the flapping and folding frequencies end up approximately the same order of magnitude regardless of length scale.

4. Results and discussion

4.1. Experimental results

We study wing-unfolding motion experimentally by varying flapping frequencies, wing geometries, and release time. Higher flapping frequencies result in faster wing unfolding in absolute time, but have little effect on the relative unfold time within a flap period. Release timing and geometry do not have large effects on unfold time.

4.1.1. Wing release timing

The phase of the wing stroke at release does not significantly affect the overall unfold time. However, it is desirable to release the wings such that they will be fully unfolded during the downstroke to improve efficiency. Therefore, we release the wings at the beginning of the downstroke to see how release phase affects unfold time and motion. We find that wing unfolding kinematics is very similar for different release phases during or near to the start of the downstroke (at 0, 2%, and −5%, figure 6). For all these trials we find that wing unfolding slows down for a moment during stroke reversal. During these transitions, the flapping velocity approaches zero as the wing reverses direction. Hence, the centrifugal accelerations become very small and non-inertial terms including aerodynamic, gravity, internal spring, and friction forces become temporarily more dominant.

Ideally the hand wing is able to fully unfold within half a wingbeat, which would eliminate the transitions between up and down stroke. Adjusting the flapping amplitude (figure 7) or using springs to act like tendons could accomplish this. However, adjusting release phase and flapping frequency do not change the relative unfold time.

4.1.2. Effects of flapping frequency and fold ratio on unfolding

Flapping frequency has the largest effect on the unfold trajectories in absolute time; the wings unfold faster in absolute time at higher flapping frequencies. Higher flapping frequencies generate higher velocities (proportional to frequency) and accelerations (proportional to frequency squared) (equation 3), leading to faster unfold times. In addition, the relative unfold speed appears to slightly increase for higher flapping frequencies between 5 and 11 Hz (figure 8). One reason for this may be friction in the wrist joint, which may slow wing unfolding at slower flapping frequencies. This hypothesis is supported by our observation that wings occasionally got stuck and didn't fully unfold at 5 Hz, but they always unfolded at 14 and 17 Hz. Flapping frequency does not affect the final position to which the wings unfold.

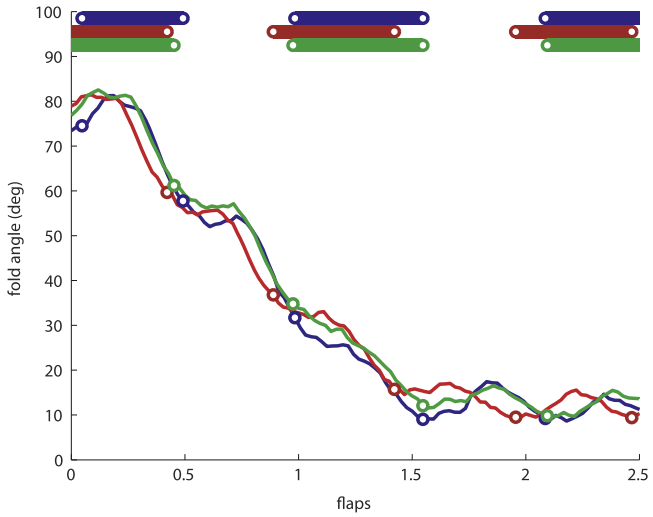

Figure 6. For identical wings and flapping frequencies, unfolding is unaffected by small differences in release phase (0% (green), 2% (red), 5% (blue)) either slightly before or slightly after the peak upstroke. The total time to unfold is approximately 1.5 flaps ($f = 14$ Hz, $FR = 2.5$). Near stroke reversal we observe a pause in the unfolding process, which we attribute to the temporarily near-zero flapping angular velocity.

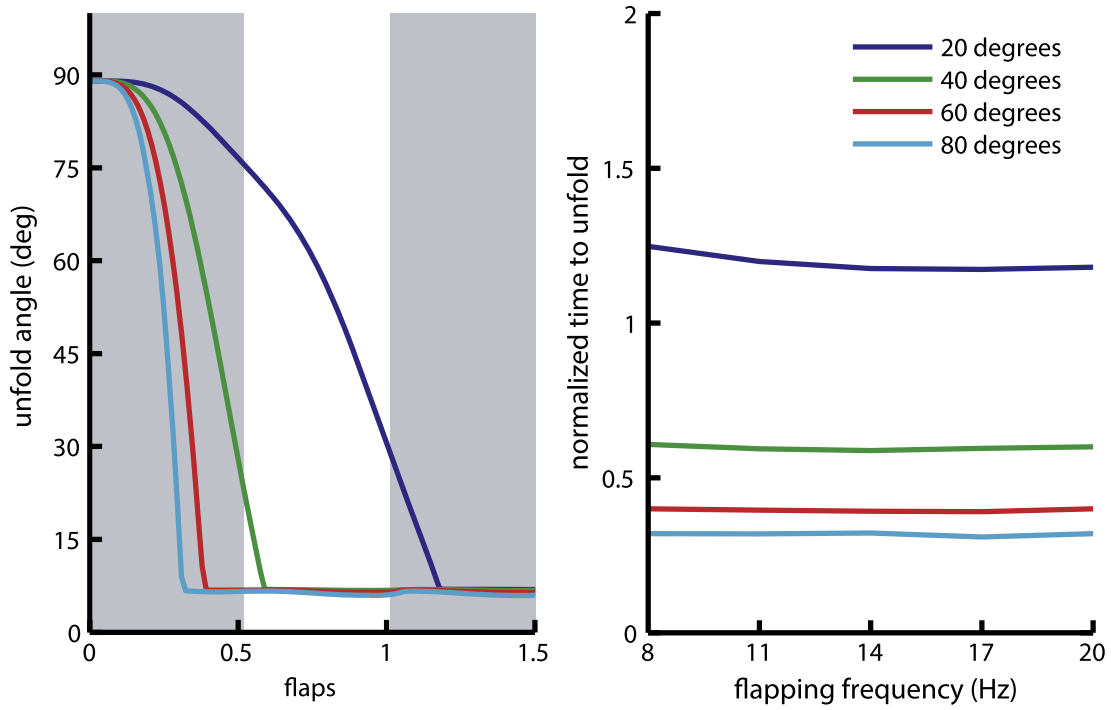

Figure 7. Changing flapping frequency has little effect on the normalized time to unfold, while changing flapping amplitude has a significant effect. Increasing the flapping amplitude beyond 60° or so will result in wing unfold times within half a flap. This is approximately the flapping amplitude used by hovering animals, while those flying forward tend to flap their wings at smaller amplitudes.

Wings with larger fold ratio (relatively large hand wing) more fully unfold, reaching a steady oscillation at a fold angle closer to zero degrees. This enhances the ability of wings with a large fold ratio to reach larger differences in folded versus unfolded size as they more closely reach their fully unfolded state. This is likely due to the extra mass present in the larger hand wings that help overcome friction effects. However, fold ratio does not significantly affect the time to unfold.

Flap angle was controlled by a DC brushed motor connected to an identical four bar mechanism in each trial, therefore, it is not surprising that the flap angle trajectories are very similar. The flap angle curves are slightly sharper than a sine curve (mean $R^2 = 0.93$ for a

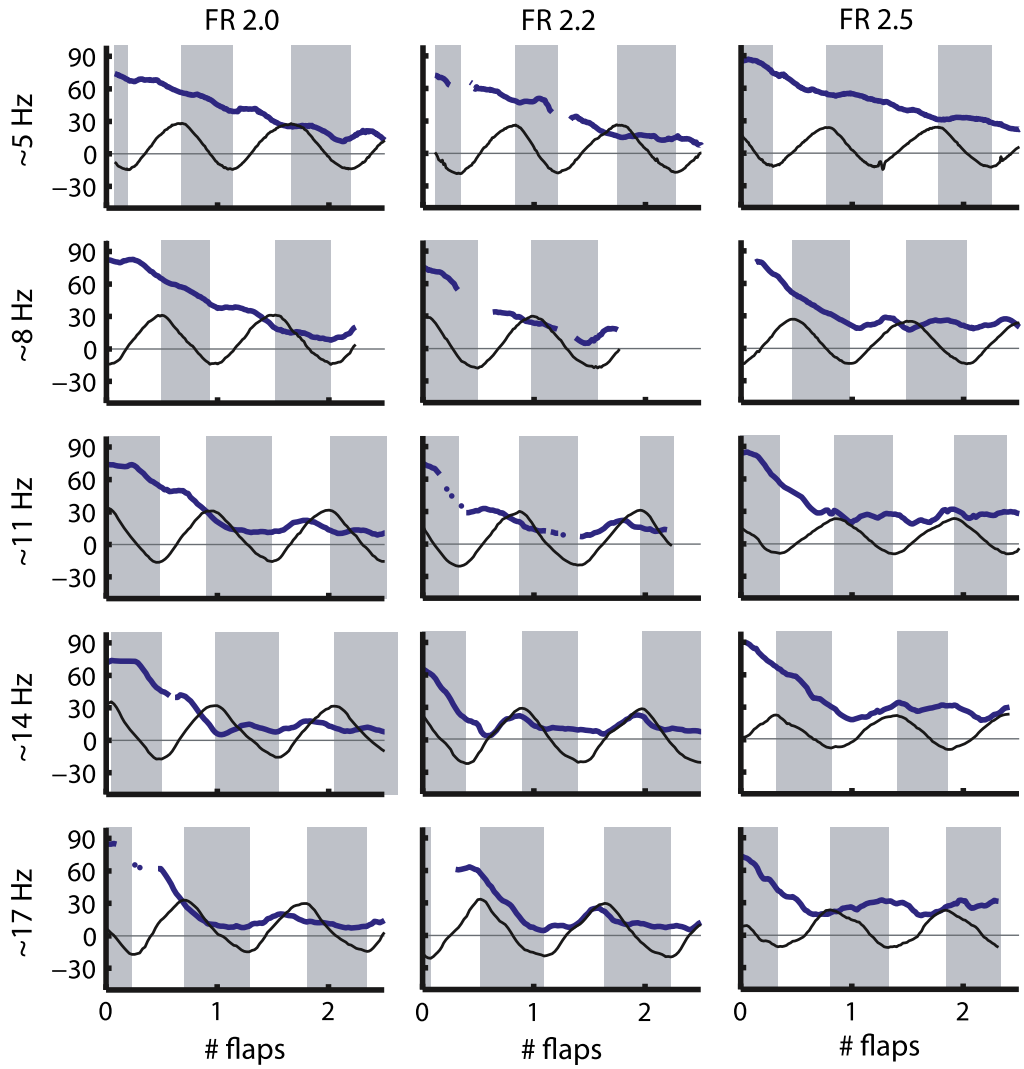

Figure 8. Under all tested conditions, wings unfold within two flaps. The wings with larger fold ratios tend to unfold more fully in addition to having more drastic reductions in wingspan. At slower flapping frequencies, wings take a slightly longer time to unfold (blue line), even normalized by flapping period. Flap angle (black line) tends to be sinusoidal regardless of folding ratio or flapping frequency. For all parameters, the flapping angle is approximately sinusoidal (20.3 degrees amplitude).

sinusoid, mean amplitude 20.4 degrees, mean offset angle 6.3 degrees), which is expected for a four bar mechanism (Berkof 1973).

4.2. Comparison of measurements and simulations of unfolding

Both the physical and simulated model wings unfold in one to one and a half flaps with an initial steep slope (figure 9). The main difference is that the experiment does so with pausing at the ends of the stroke where the flapping velocity is small, while the model continues to unfold in these regions. This is probably due to friction in the joint and Mylar stretching, which are difficult to model precisely. Even after lubricating the joints, the wing still pauses during stroke reversal, whereas we do not see this in our simulation. In the physical model, this pause cannot be overcome by the centrifugal acceleration induced by flapping, because it is too small during stroke reversal.

Neither the physical nor simulated model wings unfold all the way to zero degree sweep. In the model, this is due to imposing a contact condition at a small angle (seven degrees). This threshold represents the observed resistance to unfolding measured in the physical model due to Mylar stretching.

The unfolded physical wing oscillates slightly back and forth at the fully unfolded position, in contrast to the simulated wing, which reaches a steady angle. This is likely due to two phenomena, (1) the Mylar acting as a spring during unfolding, and (2) the decreased flapping velocity during stroke reversal. When flapping velocity decreases the 'Mylar spring' retracts the wing slightly, resulting in a small amplitude fold angle modulation. This is an undesirable feature that could be avoided in future robots by adding a torsional spring or rubber band to pull the wing toward the unfolded position.

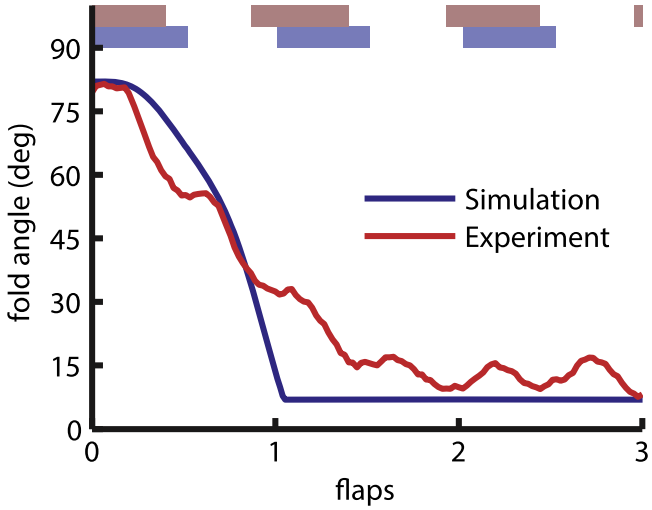

Figure 9. Both the physical and numerical model wing initially unfold quickly and then stay relatively constant at their unfolded equilibrium position. However, the physical model does not reach zero degrees fold angle and needs more time to reach its fully unfolded position. The physical model also exhibits small pauses in unfolding during stroke reversal, which is not captured by the simulation.

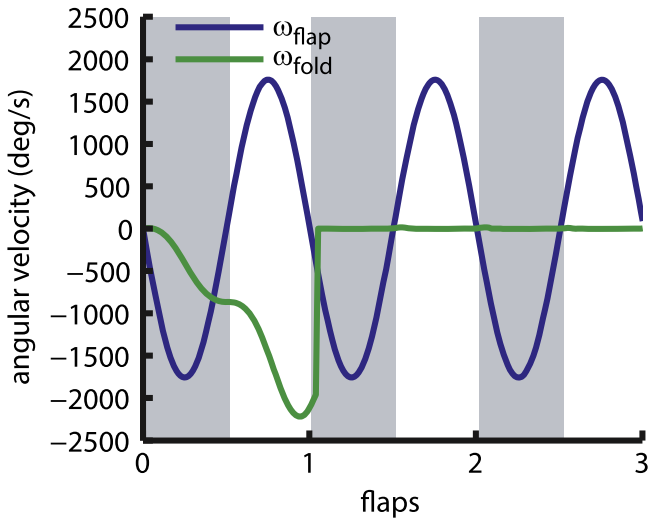

Figure 10. Folding and flapping angular velocity as a function of flapping period. During the unfolding period these velocities have similar magnitudes, after which the folding angular velocity decreases to approximately zero when the wing is unfolded.

4.3. Simulation results

We use simulations to examine how the different forces and accelerations that act on the flapping wing affect its unfolding performance. We focus our comparisons on unfolding wings with a fold ratio of 2.5, which is the largest reduction in wingspan of the wings we tested, and a flapping frequency of 14 Hz, which is the frequency needed for sustained hover of a DelFly sized flapper.

4.3.1. Angular velocity of fold and flap angles during unfolding

The simulation of wing unfolding confirms the angular velocities are comparable in magnitude to the flapping angular velocity (figure 10). The simulations show the angular velocity stops increasing in magnitude during stroke reversal, which caused the unfolding of the physical wing to stutter. This decrease in flapping velocity at stroke reversal is inevitable if the wing is to flap instead of spin. For a more consistent unfolding velocity, it would be necessary to add a component that can store and release energy like a spring, such that the wing fold angular acceleration remains negative throughout the stroke.

4.3.2. Effect of aerodynamic force versus flapping and gravity induced accelerations

The largest contribution to induced acceleration comes from the flapping motion. Smaller contributions come from gravity and aerodynamic forces. When the simulation reaches the unfolded position, contact forces are introduced, which are shown

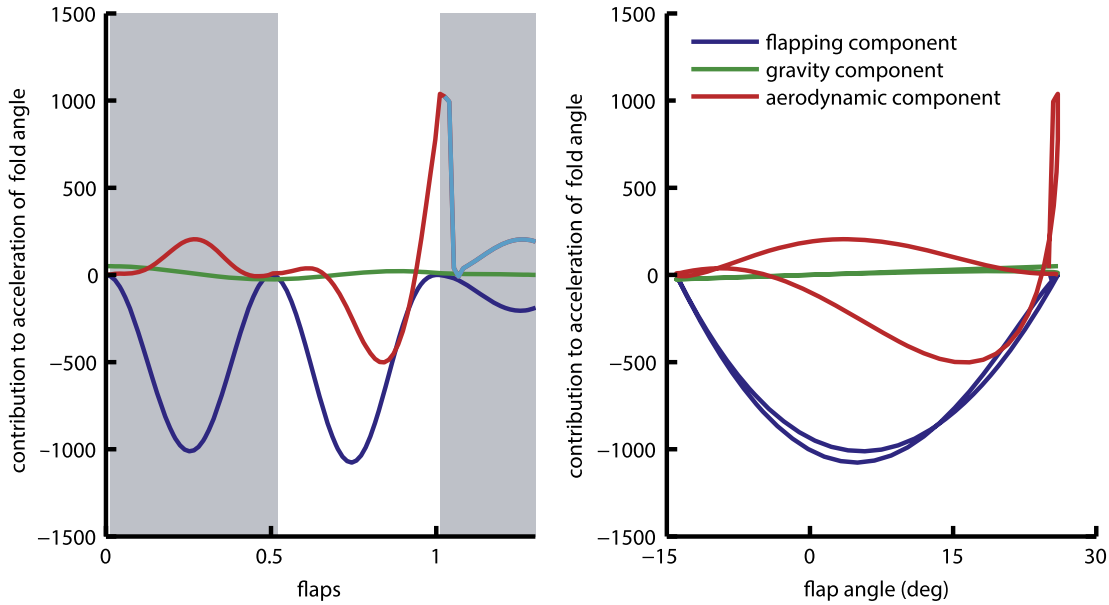

Figure 11. Flapping terms dominate the unfolding acceleration. The flapping terms are fundamentally negative, causing them to always accelerate unfolding. Negative accelerations promote unfolding, as they result in more negative unfolding velocity, and thus smaller fold angle. Positive accelerations hinder unfolding. Gravity and aerodynamic contributions are much smaller. Note: red line changes to cyan to indicate combined aerodynamic and contact forces when the wing comes in contact with the joint at the fully unfolded position.

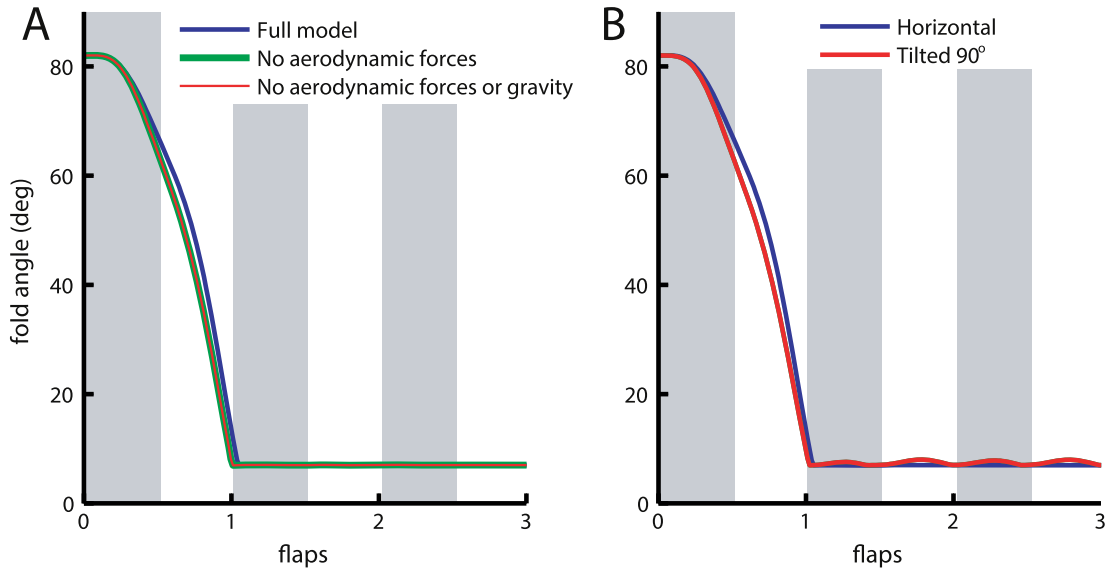

Figure 12. The model shows that unfolding time is driven by flapping induced accelerations. (A) Gravitational and aerodynamic effects are negligible. Removing aerodynamics causes the unfold time to decrease somewhat, as drag no longer slows it down. Removing gravity has very little effect (obscured thin red line). (B) Pitching the model nose up to 90° leads to insignificant differences compared to horizontal—confirming that wing unfolding is driven by centrifugal accelerations and not hindered by gravity.

combined with the aerodynamic components in figure 11 (The components due to flapping and gravity are calculated from the analytic equations derived in equation 3).

The centrifugal acceleration due to flapping depends on flapping angular velocity squared. Therefore, non-zero centrifugal acceleration is always helpful to the unfolding process. As expected, it peaks at mid-stroke, and reduces to zero at stroke reversal. This is the primary component which causes the wings to unfold.

The aerodynamic forces have a much smaller magnitude than the flapping induced centrifugal accelerations (figure 11 and figure 12). By definition, drag force always opposes motion of the wing, and thus hinders the unfolding process. Lift force, on the other

hand, helps in the unfolding process and helps keep the wing unfolded. We also observe unfolding even when the Mylar film is removed leaving only the leading edges of the wings (as in figure 5(A)), which corroborates the hypothesis that aerodynamic effects are not critical for unfolding.

The least significant contribution to the wing's unfolding is gravity. It is also not directly controllable or removable from the system and oscillates between helping and hindering the unfolding process depending on the wingbeat phase (figure 11). However, its net effect on unfolding time and shape is very small and insignificant for sufficiently fast flapping wings (figure 12). As this component is purely geometric, it has the same effect during up and down stroke. When the robot is pitched up, wing unfolding is similar (~1° deviation), showing that gravity effects can be ignored and that wing unfolding is driven primarily by centrifugal acceleration (figure 12). In pitch down configurations, gravity helps the unfolding process.

4.3.3. Effects of removing aerodynamic or gravity forces on unfold timing

Since it seems wing unfolding depends mostly on flapping induced centrifugal accelerations, we simulated the effect of removing aerodynamic and gravitational forces on wing unfolding (figure 12). Without aerodynamic forces, the wing unfolds slightly faster. This is reasonable as the drag force hinders the unfolding process, while the lift force promotes unfolding, but not significantly compared to the centrifugal accelerations induced by flapping. Removing gravity has little to no effect on unfolding, as predicted by our order of magnitude analysis. Tilting the robot so that gravity hinders unfolding also has little effect on the final position reached.

4.3.4. Effects of changing flapping frequency or flapping amplitude on unfold timing

It is desirable to control the unfold time of a robot. For a given wing design only the flapping frequency and flapping amplitude can be changed, of which we simulated the effect on unfolding time (figure 7).

For a given flapping amplitude, higher flapping frequencies lead to a faster unfold time. This is reasonable, as the induced centrifugal accelerations are correlated with the flapping velocity. However, when normalized by the flapping period, this effect was very small, and not easy to measure in a physical implementation.

Increasing the flapping amplitude speeds up wing unfolding, because larger flapping amplitudes cause larger centrifugal accelerations for a given flapping frequency. The effect of an increase in flapping amplitude on unfolding time is largest for small amplitudes, but remains significant for large flapping amplitudes. If the flapping amplitude of our robot is increased beyond roughly 60°, then passive unfolding will take place within half a flap.

Large flapping amplitude not only decreases the normalized and absolute unfold times, it also increases aerodynamic efficiency, because of the higher actuator disk area, which results in a lower disk loading, and thus higher Froude efficiency (Froude 1883). Further, the positive effect of wing amplitude on the unfolding time suggests that a vehicle with a single pair of flapping wings has an advantage over a bi-plane configuration, because the flapping amplitude of a biplane will always be approximately a factor two smaller. Hence, the time for passive unfolding will be much shorter for a single pair of wings flapping at high amplitude. This quick unfolding also provides a mechanism to quickly recover the hand wing position after hard impact with a branch or other object by simply flapping the wing to unfold it again.

4.4. Recovery from obstacle impact

The passively unfolding mechanism allows the robot to temporarily morph its hand wing to accommodate a rigid impact. This is similar to how the flexible feathers of a bird hand wing or the costal break in a wasp wing (Mountcastle and Combes 2014) allow for impact with obstacles without significantly affecting structural integrity. In our robot, the hinged joint allows the hand wing to comply with the obstacle during impact. After impact, the flapping motion causes the wing to re-extend to its full wingspan. This occurs without requiring actuators or control electronics, making it a very lightweight and reliable solution.

The ability to deform and then recover from a sudden impact (hit with 7 mm diameter steel rod) occurs at both low (figure 13) and high (figure 14) flapping frequencies and impact velocities. At low velocities (~2 m s^{-1}, ~8 Hz), the wings remain in contact with the obstacle and then immediately unfold following the removal. At higher velocities (~5 m s^{-1}, ~14 Hz), the wing deforms more significantly from the impact, but still recovers in a short period of time (0.2 s from A to D, figure 14). During the impact and recovery process there was no damage to the robot.

4.5. Applications to animal flight

Birds and bats can modulate their wingspan during flapping flight through some combination of musculoskeletal action and inertial dynamics. Our model predicts that animals with flapping wings can passively unfold their wing during the downstroke and after collisions by simply flapping their wings with their major up and downstroke muscles (and modulating the details using the much smaller hand and arm wing muscle groups). We hypothetically determined how quickly different bird, bat, and insect species could unfold their wings relying strictly on passive centrifugal accelerations induced by wing flapping. Typical flapping amplitudes and fold ratios of birds correspond with predicted passive unfolding times of approximately 0.5–0.9 wingbeats according to our

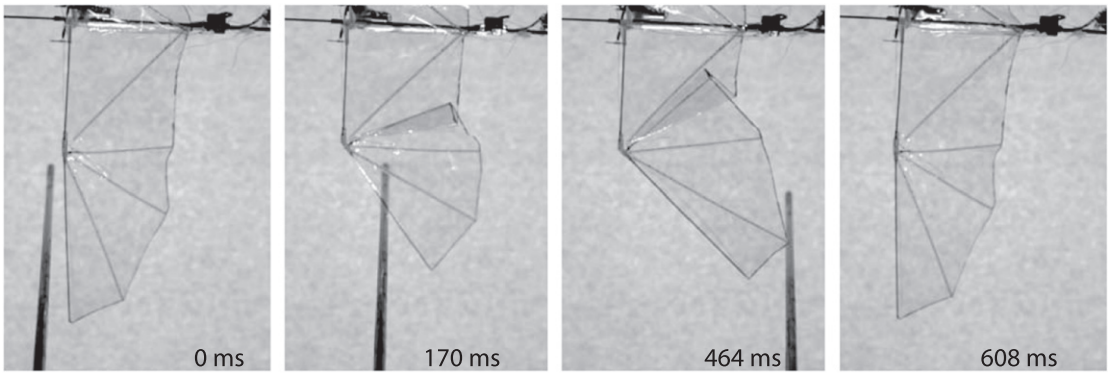

Figure 13. Impact resistance at slow obstacle speed (~2 m s^{-1}) and slow flapping frequency (~8 Hz, flapping period ~125 ms). Obstacle leaves frame in the final frame. When the obstacle first hits the wing, it deforms, but after the obstacle passes the wing returns to its open configuration (high-speed video at 500 fps).

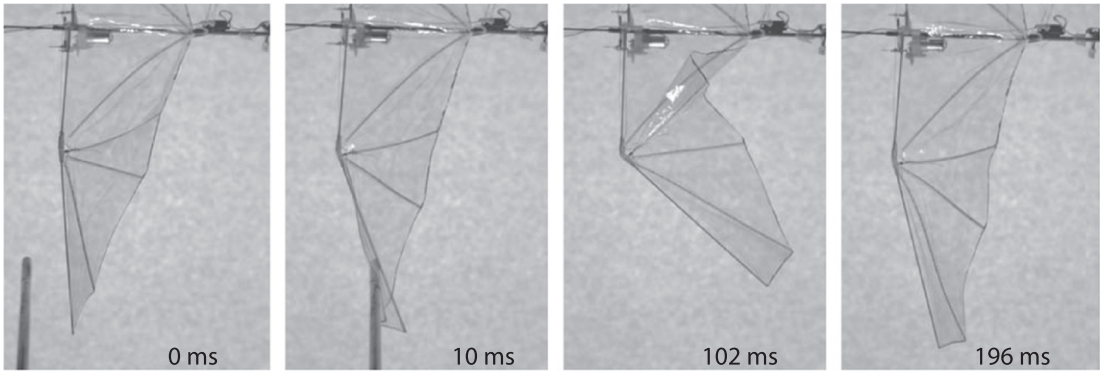

Figure 14. Impact resistance at fast obstacle speed (~5 m s^{-1}) and fast flapping frequency (~14 Hz, flapping period ~71 ms). Obstacle has moved out of view in the final two frames. The wing deforms more, but still restores itself to the unfolded position within a few flaps (high-speed video at 500 fps).

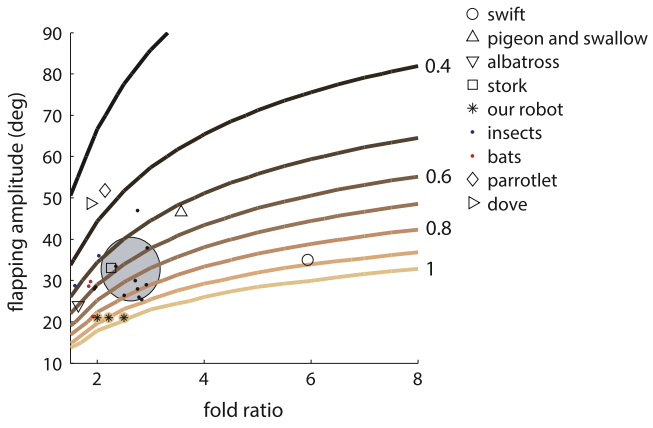

Figure 15. Passive unfold times predicted by our dynamic model for several birds, bats, insects, and our robot based on wing fold ratio and flapping amplitude. Contour lines indicate constant unfold times predicted by the model. Gray circle represents mean and standard deviation of fold ratio and flapping amplitude for birds (standard deviations calculated from 46 bird species for flapping amplitude and 248 species for fold ratio). Colored dots around robot markers indicate measured robot normalized unfolding time. For 16 species both values were available and are plotted on the graph. Contours represent predicted normalized unfold time. Flapping amplitudes from: (Nudds *et al* 2004, Norberg 1975, Mountcastle and Combes 2014), wing dimensions from: (Tobalske and Dial 1996, Corvidae *et al* 2006, Norberg 1986, Greenewalt 1962, Mountcastle and Combes, 2014, Aldridge 1987). Estimates for the dove were obtained from high speed video from the Flight Artists outreach project (Hoebink and van der Sar 2012). Data for the Pacific parrotlet *Forpus coelestis* was obtained with high speed video at 1000 fps (Phantom M310). The parrotlet was trained using positive reinforcement, food and water was provided *ad libitum*, and all training and experimental procedures were approved by Stanford's Administrative Panel on Laboratory Animal Care.

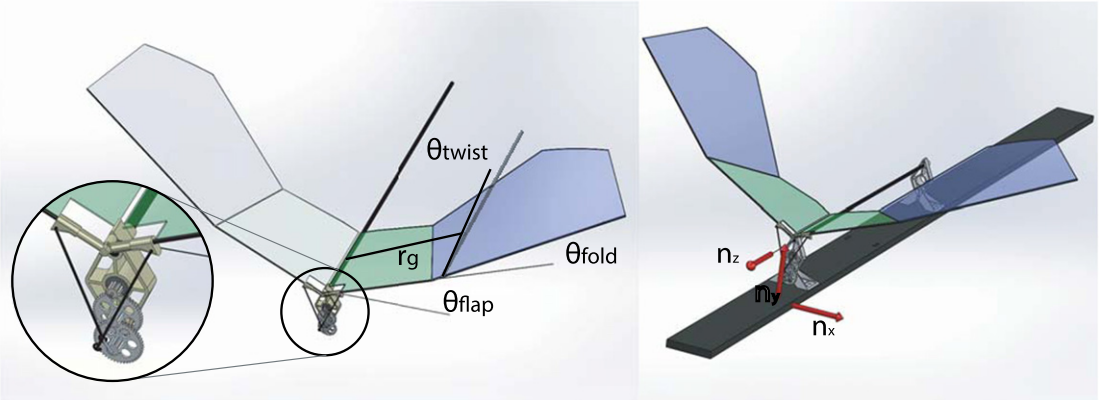

Figure 16. Left: a four bar mechanism driven by a small helicopter motor connected to a gearbox controls the flap angle. Right: angle conventions used in the simulation. For simulation, we assume the flap and twist angles vary sinusoidally out of phase with each other. We apply approximations of the aerodynamic forces at the quarter chord at the radius of gyration, based on specified wing geometric angle of attack and wing flapping. From the combination of wing flapping, inertia and aerodynamics, we calculate the fold angle over time.

model (figure 15). Based on observations of forward flapping flight in parrotlets (~20 Hz) and doves (~10 Hz), we estimate that flapping bird wings unfold within approximately 0.25–0.5 flaps. While passive centrifugal unfolding cannot account for all of this; it is close enough to suggest that passive wing unfolding and plays a significant role. This is particularly true for smaller birds, such as the parrotlet (wingspan 0.205 m) in which flapping amplitude tends to be larger (Nudds *et al* 2004) which decreases unfold time. We thus predict that the hand and arm wings muscles' primary function during flapping flight is to fold the wing, unfolding can be facilitated largely by centrifugal acceleration induced by the primary flight muscles wingbeat. Whereas the passive wing unfolding mechanism demonstrated here probably alleviates the muscle effort needed to unfold dynamically during a stroke—folding requires more effort as a result. We hypothesize that birds might be able to modulate this energetic trade-off through recruitment of muscles and energy storage in tendons. In robots we envision the use of energy storage devices, such as tuned springs, to potentially enable closer replication of the continuous wing morphing birds employ during flapping flight. Such dynamic wing morphing might help improve aerodynamic efficiency by minimizing drag during the upstroke during forward flight.

5. Conclusions

The results presented here show that centrifugal accelerations induced by wing flapping allow robotic wings to passively unfold about a wrist joint. The wings unfold back to their full wingspan configuration both when released from a folded position and when deflected by a colliding obstacle. Our dynamic model predicts the passive wing unfolding behavior. These simulations indicate that unfolding is dominated by centrifugal accelerations induced by wing flapping rather than aerodynamic or gravitational forces. Experiments suggest that friction in the hinge should be minimized to the largest extent possible. The predicted unfold time based solely on centrifugal acceleration is on the order of one wingbeat and can be as short as half a wingbeat, or faster at flapping amplitudes beyond 60°. We observe unfolding times of up to approximately two wingbeats during obstacle impact. Dimensional analysis suggests that relative unfold time is independent of length scale.

Our results predict that unfolding flapping bat and bird wings might benefit from the here demonstrated passive wing unfolding mechanism. This insight, corroborated from the theoretical, numerical and physical analysis of a flapping folding wing, provides new research avenues for the functional interpretation of the muscle groups that control vertebrate hand and arm wings. Applications range from future flapping morphing wings that change shape as fluidly as bird wings, to flapping wings that can automatically recover after hard impacts during flight through clutter.

Acknowledgments

This project is supported by Office of Naval Research (ONR) Multidisciplinary University Research Initiative (MURI) grant N00014-09-1051. We thank Eirik Ravnan for making the parrotlet video recordings.

Appendix

A.1. Computing the flap and fold angles

Using markers attached to the wings, we produced three reference vectors; a vertically upward reference vector ($\hat{n}_y$), a reference vector from the rear to the front of the body ($\hat{n}_z$), and a horizontal vector to form a right handed coordinate system ($\hat{n}_x$) (figure 16). Points along the leading edge and wing spars of the left

wing allowed calculation of flapping and folding angles. We fit a vector, $\boldsymbol{v}_{\text{inner}}$, through the points along the leading edge of the arm wing and a second vector, $\boldsymbol{v}_{\text{outer}}$, through the points along the leading edge of the hand wing. The flap angle was calculated as the angle between the vector along the arm leading edge and the horizontal:

$$\theta_{\text{flap}} = \text{acos}\left(\frac{\left(\hat{n}_x \cdot \boldsymbol{v}_{\text{inner}}\right)}{\left|\hat{n}_x\right|\left|\boldsymbol{v}_{\text{inner}}\right|}\right). \quad (12)$$

The fold angle was then calculated as the angle between the arm and hand leading edge vectors in the plane spanned by the body and the arm leading edge vector. The hand leading edge vector was assumed to lie in the same plane as the plane formed by the body and the arm leading edge vector, and this was verified to be true from sample data sets:

$$\theta_{\text{fold}} = \text{acos}\left(\frac{\left(\boldsymbol{v}_{\text{outer}} \cdot \boldsymbol{v}_{\text{inner}}\right)}{\left|\boldsymbol{v}_{\text{outer}}\right|\left|\boldsymbol{v}_{\text{inner}}\right|}\right). \quad (13)$$

The release time was calculated from either the point the LED turned on or back calculated from the point the servo stopped moving according to camera measurements. The release time was subsequently subtracted from the measurements such that release occurred at time zero.

References

Aldridge H 1987 Body accelerations during the wingbeat in six bat species: the function of the upstroke in thrust generation *J. Exp. Biol.* **130** 275–93

Altshuler D L, Quicazan-Rubio E M, Segre P S and Middleton K M 2012 Wingbeat kinematics and motor control of yaw turns in Anna's hummingbirds (*Calypte anna*) *J. Exp. Biol.* **215** 4070–84

Bahlman J W, Swartz S M and Breuer K S 2013 Design and characterization of a multi-ariculated robotic bat wing *Bioinsp. Biomim.* **8** 016009

Berkof R S 1973 Complete force and moment balancing of inline four-bar linkages *Mech. Mach. Theory* **8** 397–410

Bridges T J and Georgiou K V 2001 A transverse spinning double pendulum *Chaos Solitons Fractals* **12** 131–44

Bruggeman B 2010 Improving flight performance of DelFly II in hover by improving wing design and driving mechanism *Master's Thesis* Delft University of Technology, The Netherlands

Carruthers A C, Thomas A L and Taylor G K 2007 Automatic aeroelastic devices in the wings of a steppe eagle *Aquila nipalensis J. Exp. Biol.* **210** 4136–49

Colorado J, Barrientos A, Rossi C and Breuer K S 2012 Biomechanics of smart wings in a bat robot: morphing wings using SMA actuators *Bioinsp. Biomim.* **7** 036006

Colorado J, Barrientos A, Rossi C and Parra C 2012 Inertia attitude control of a bat-like morphing-wing air vehicle *Bioinsp. Biomim.* **8** 016001

Corvidae E L, Bierregaard R O and Peters S E 2006 Comparison of wing morphology in three birds of prey: correlations with differences in flight behavior *J. Morphol.* **267** 612–22

Deng X, Schenato L, Wu W C and Sastry S S 2006 Flapping flight for biomimetic robotic insects: I. System modeling *IEEE Trans. Robot.* **22** 776–88

Deters R W and Selig M S 2008 *Static Testing of Micro Propellers* (Honolulu: AIAA Applied Aerodynamics Conference)

Dickinson M H, Lehmann F-O and Sane S P 1999 Wing rotation and the aerodynamic basis of insect flight *Science* **284** 1954–60

Dickinson W B, Straw A D and Dickinson M H 2008 Integrative model of drosophila flight *AIAA J.* **46** 2150–64

Froude R E 1883 A description of a method of investigation of screw-propeller efficiency *Trans. Inst. Naval Architects* **24** 231–55

Gilardi G and Sharf I 2002 Literature survey of contact dynamics modeling *Mech. Mach. Theory* **37** 1213–39

Grant D T, Abdulrahim M and Lind R 2010 Design and analysis of biomimetic joints for morphing of micro air vehicles *Bioinsp. Biomim.* **5** 045007

Grant D T, Abdulrahim M and Lind R 2006 *Flight Dynamics of a Morphing Aircraft Utilizing Independent Multiple-Joint Wing Sweep* (Keystone, CO: AIAA Atmospheric Flight Mechanics Conference and Exhibit)

Greenewalt C H 1962 *Dimensional Relationships For Flying Animals* (Washington DC: Smithsonian Miscellaneous Collections)

Hedrick T L 2008 Software techniques for two- and three-dimensional kinematic measurements of biological and biomimetic systems *Bioinsp. Biomim.* **3** 034001

Hedrick T L and Biewener A A 2007 Low speed maneuvering flight of the rose-breasted cockatoo (*Eolophus roseicapillus*). I. Kinematic and neuromuscular control of turning *J. Exp. Biol.* **210** 1897–911

Hedrick T L, Usherwood J R and Biewener A A 2007 Low speed maneuvering flight of the rose-breasted cockatoo (*Eolophus roseicapillus*). II. Inertial and aerodynamic reorientation *J. Exp. Biol.* **210** 1912–24

Hoebink W and van der Sar X 2012 Dove as angel www.youtube.com/watch?v=9RmaVl4Sw0Y (retrieved 5 September 2014)

Keennon M, Klingebiel K, Won H and Andriukov A 2012 Tailless flapping wing propulsion and control development *American Helicopter Society 68th Annual Forum* (*Fort Worth, TX*) (*AHS*)

Lentink D L *et al* 2007 How swifts control their glide performance with morphing wings *Nature* **446** 1082–5

Lentink D, Jongerius S R and Bradshaw N L 2009 The scalable design of flapping micro aerial vehicles inspired by insect flight *Flying Insects and Robots* (Berlin: Springer) pp 185–205

MacKenzie P M and Forrester M A 2008 Sailboat propeller drag *Ocean Eng.* **35** 28–40

Maxwell J C 1867 On governors *Proc. R. Soc. London* **16** 270–83

Mountcastle A M and Combes S A 2014 Biomechanical strategies for mitigating collision damage in insect wings: structural design versus embedded elastic materials *J. Exp. Biol.* **217** 1108–15

Norberg U M 1986 Evolutionary convergence in foraging niche and flight morphology in insectivorous aerial hawking birds and bats *Ornis Scandinavia* **17** 253–60

Norberg U M 1975 Hovering flight in the pied flycatcher (*Ficedula hypoleuca*) ed T T Wu *Swimming and Flying in Nature* (New York: Springer) pp 869–81

Nudds R L, Taylor G K and Thomas A L 2004 Tuning of Strouhal number for high propulsive efficiency accurately predicts how wingbeat frequency and stroke amplitude relate and scale with size and flight speed in birds *Proc. R. Soc. Biol. Sci.* **271** 2071–6

Pennycuick C J 1968 A wind-tunnel study of gliding flight in the pigeon *Columba livia J. Exp. Biol.* **49** 509–26

Pennycuick C J 2008 The feathered wings of birds *Modelling the Flying Bird* ed C J Pennycuick (Amsterdam: Elsevier) pp 105–34

Pennycuick C J 2008 The membrane wings of bats and pterosaurs *Modelling the Flying Bird* ed C J Pennycuick (Amsterdam: Elsevier) pp 135–60

Smith W R and Norwell J S 1889 *Illustrations of Zoology: Invertebrates & Vertebrates* (Edinburgh: Pentland)

Song A *et al* 2008 Aeromechanics of membrane wings with implications for animal flight *AIAA J.* **46** 2096–106

Swartz S M, Iriarte-Diaz J, Riskin D K, Song A, Tian X, Willis D J and Breuer K S 2007 Wing structure and the aerodynamic basis of flight in bats *Proc. 45th AIAA Aerospace Sciences Meeting and Exhibit* (*Reno, NV 2007*) (American Institute of Aeronautics and Astronautics Aerospace Sciences) vol 45 pp 22–26

Taylor G K, Carruthers A C and Hubel T Y 2012 Wing morphing in insects, birds and bats: mechanism and function *Morphing Aerospace Vehicles and Structures* ed J Valasek (New York: Wiley) pp 11–40

Team Roboswift 2007 Roboswift technical fact sheet www.roboswift.nl/images/RoboSwift_Technical_Factsheet.pdf (retrieved 12 March 2014)

Tobalske B W and Dial K P 1996 Flight kinematics of black-billed magpies and pigeons over a wide range of speeds *J. Exp. Biol.* **199** 263–80

Wissa A A, Tummala Y, Hubbard J E Jr and Frecker M I 2012 Passively morphing ornithopter wings constructed using a novel compliant spine: design and testing *Smart Mater. Struct.* **21** 094028